Noncontact 3-D Speckle Contrast Diffuse Correlation Tomography of Tissue Blood Flow Distribution

Chong Huang, Daniel Irwin, Mingjun Zhao, Yu Shang, Nneamaka Agochukwu, Lesley Wong, and Guoqiang Yu

Abstract—Recent advancements in near-infrared diffuse correlation techniques and instrumentation have opened the path for versatile deep tissue microvasculature blood flow imaging systems. Despite this progress there remains a need for a completely noncontact, noninvasive device with high translatability from small/testing (animal) to large/target (human) subjects with trivial application on both. Accordingly, we discuss our newly developed setup which meets this demand, termed noncontact speckle contrast diffuse correlation tomography (nc_scDCT). The nc_scDCT provides fast, continuous, portable, noninvasive, and inexpensive acquisition of 3-D tomographic deep (up to 10 mm) tissue blood flow distributions with straightforward design and customization. The features presented include a finite-element-method implementation for incorporating complex tissue boundaries, fully noncontact hardware for avoiding tissue compression and interactions, rapid data collection with a diffuse speckle contrast method, reflectance-based design promoting experimental translation, extensibility to related techniques, and robust adjustable source and detector patterns and density for high resolution measurement with flexible regions of interest enabling unique application-specific setups. Validation is shown in the detection and characterization of both high and low contrasts in flow relative to the background using tissue phantoms with a pump-connected tube (high) and phantom spheres (low). Furthermore, *in vivo* validation of extracting spatiotemporal 3-D blood flow distributions and hyperemic response during forearm cuff occlusion is demonstrated. Finally, the success of instrument feasibility in clinical use is examined through the intraoperative imaging of mastectomy skin flap.

C. Huang, D. Irwin, M. Zhao, and G. Yu are with the Department of Biomedical Engineering, University of Kentucky, Lexington, KY 40506 USA (e-mail: guoqiang.yu@uky.edu).

Y. Shang is with the Department of Biomedical Engineering, University of Kentucky, Lexington, KY 40506 USA, and also with the Key Laboratory of Instrumentation Science and Dynamic Measurement, North University of China, Taiyuan 030051, China.

N. Agochukwu and L. Wong are with the Division of Plastic Surgery, University of Kentucky, Lexington, KY 40536 USA.

Index Terms—Finite element modeling, image reconstruction-iterative methods, optical imaging, perfusion imaging, system design.

I. Introduction

ALTERATIONS in blood flow may result in regional tissue ischemia and hypoxia. Imaging of regional flow abnormalities can help characterize many diseases associated with tissue ischemia and hypoxia including wounds, stroke, and cancer. Furthermore, perioperative imaging of tissue blood flow distribution can assist in therapeutic monitoring of those diseases and interventions. In contrast to large imaging modalities such as CT, MRI, and PET, optical imaging instruments are portable, fast, continuous, inexpensive, and noninvasive. Optical techniques based on dynamic light scattering are the most common methods for blood flow measurements in tissue microvasculature including laser speckle contrast imaging (LSCI) [1], [2] and near-infrared (NIR) diffuse correlation spectroscopy/tomography (DCS/DCT) [3]–[10]. Each technique, however, has key issues that limit its application. LSCI uses wide-field illumination and charge-coupled-device (CCD) detection of spatial and/or temporal speckle contrasts to achieve rapid high-resolution two-dimensional mapping of blood flow in superficial tissues (depth < 1 mm) [1], [2], [11], [12]. LSCI systems are typically limited in probing information from deeper tissues. By contrast, DCS/DCT uses coherent NIR point-source illumination and avalanche photodiode (APD) detection of temporal fluctuations of diffuse speckle contrasts in a single speckle area to accommodate spectroscopic and tomographic measurements of blood flow variations in deep tissues (up to ∼15 mm depth) [3]–[10]. The use of expensive APDs limits its spatial-temporal resolution and increases instrumentation cost.

Very recently, our group developed a reflectance diffuse speckle contrast tomography technique, namely speckle contrast DCT (scDCT) [13]. scDCT examines deep tissue blood flow by monitoring spatial (or temporal) diffuse speckle contrasts as opposed to correlation decay curves [13]–[18]. APDs were replaced by a single highly sensitive electron-multiplying CCD (EMCCD) camera with zoom lens for rapid and inexpensive measurements. Prior to scDCT there had been no diffuse speckle contrast deep flow instruments developed for three-dimensional (3D) tomography in a reflectance configuration.

This configuration more adequately represents the situation encountered in larger subjects such as humans where the transmission measurement is not practical due to the limited penetration depth of light and thus encourages clinical usage. The scDCT combines the benefits of CCD detection with our finite-element-method (FEM) based DCT reconstruction technique [9], [10], [19] allowing for 3D imaging of flow distributions in deep complex turbid media (up to ~10 mm). In scDCT, four source fibers were positioned symmetrically on a metal holder placed on the surface of the measured medium and outside the EMCCD field of view (FOV). The fibers were coupled with an optical switch for sequencing. This unique imaging system was calibrated and validated through incorporation of liquid and solid tissue-like phantoms; the solid heterogeneity (no flow) submerged below the Intralipid liquid solution (flow/particle Brownian motion) was identified successfully by reconstructed 3D flow contrast tomography with scDCT [13].

While effective, the prototype scDCT is constrained by the limited number of source fibers (n = 4) for photon emission, leading to poor sampling density. The source fibers used in this prototype device are in contact with the measured medium, reducing the flexibility of source and detector arrangement. To avoid the interference with the detection, for example, source fibers cannot be placed inside the camera FOV. Also, the contact measurement with source fibers may be disadvantaged for some *in vivo* measurement cases due to the potential infection of ulcerous/incision tissues or the distortion of tissue hemodynamics resulted from the contact/compression of the fiber-optic probe on vulnerable/soft tissues. Furthermore, in testing the scDCT system, the simulation of flow contrast relies on a solid phantom embedded in a liquid phantom, which lacks elegance due to the restrictively static nature of the components once prepared, specifically the solid phantom material [13]. Most importantly, the scDCT system has not been evaluated for *in vivo* measurements.

The current study seeks to remedy many of these concerns while leveraging the concepts from the previous systems. As a result, a fully noncontact scDCT device is developed, namely nc_scDCT. First, a galvo mirror is used to rapidly deliver NIR light in a noncontact manner to numerous source positions inside the FOV of EMCCD camera. This fully noncontact measurement design increases the possible arrangements of laser source positioning while improving sampling density as well as providing the capability of adjusting the region of interest (ROI) size for adapting to many different applications. Next, validation efforts test the ability of this reflectance-based system to achieve dynamic applicability through an improved and flexible phantom test design as well as by *in vivo* measurements. The phantoms employed promote both high and low flow contrasts. Following this validation, a human subject is monitored with nc_scDCT for forearm blood flow variation during arterial occlusion of the upper arm. Finally, a clinical case study is conducted to further demonstrate the feasibility of using the new nc_scDCT device for intraoperative imaging of mastectomy skin flaps. This progression of investigations challenges the novel system against the claim of adapting
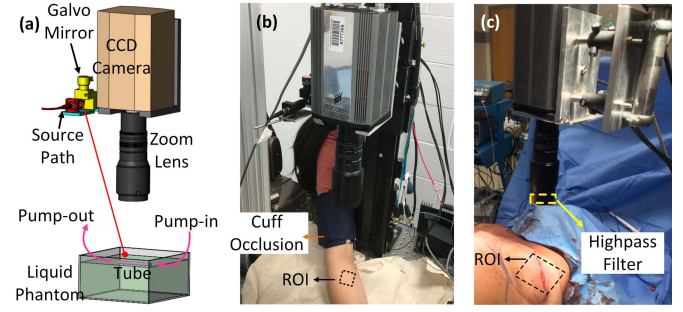

Fig. 1. The nc_scDCT instrument and experimental setups for 3D flow imaging. (a) In the first heterogeneous phantom, a transparent cylindrical tube, connected with a peristaltic pump, was placed at ~5 mm below the liquid phantom surface to create high flow contrasts against the background. In the second heterogeneous phantom, two spherical solid phantoms were placed at ~5 mm below the liquid phantom surface at different locations to create low flow contrasts. (b) Blood flow changes in a healthy human forearm induced by the arterial cuff-occlusion on subject's upper arm were continuously imaged by nc_scDCT. (c) A mastectomy skin flap imaged by nc_scDCT intraoperatively. An 800-nm high-pass filter minimizes the influence of ambient light in the operating room after moving away the lamp beam from the breast. For laboratorial experiments, the room was kept dark.

to large and small regions with quality 3D flow distribution information.

II. METHODS

A. The nc_scDCT System

Fig. 1 shows the nc_scDCT instrument and experimental setups for the measurements on tissue-simulating phantoms (**Fig. 1a**), a forearm (**Fig. 1b**), and a mastectomy skin flap (**Fig. 1c**). In nc_scDCT system, a highly sensitive EMCCD (Cascade 1K, Photometrics, AZ) is used to detect spatial speckle contrasts in a selected ROI and a galvo mirror (GVS002, Thorlabs, NJ) is used to deliver point-source NIR light generated from a long coherence laser (830 nm, CrystaLaser, NV) to different source positions. A zoom lens (Zoom 7000, Navitar, NY) is connected to the EMCCD camera enabling easily adjusting the size of ROI. A pair of polarizers (LPNIRE050-B and LPNIRE200-B, Thorlabs, NJ) is added crossing the source path and EMCCD detection path to reduce the light source reflection from the tissue surface. An 800-nm high-pass filter (84-762, EdmundOptics, NJ) is installed in front of the EMCCD to minimize the influence of ambient light in the operating room (**Fig. 1c**).

As described previously [13], our scDCT technique extracts blood flow index (BFI) information on the tissue boundary from the spatial distribution of diffuse laser speckles detected by the EMCCD. Briefly, spatial speckle contrast detected by the EMCCD at the position r is defined as

$$K_s(r) = \frac{\sigma_s}{\langle I \rangle} \tag{1}$$

where σ_s is the spatial standard deviation and $\langle I \rangle$ is the mean intensity in a pixel window of 7 × 7 pixels [1], [12], [13], [18], [20]. $K_s(r)$ is related to the normalized temporal electric
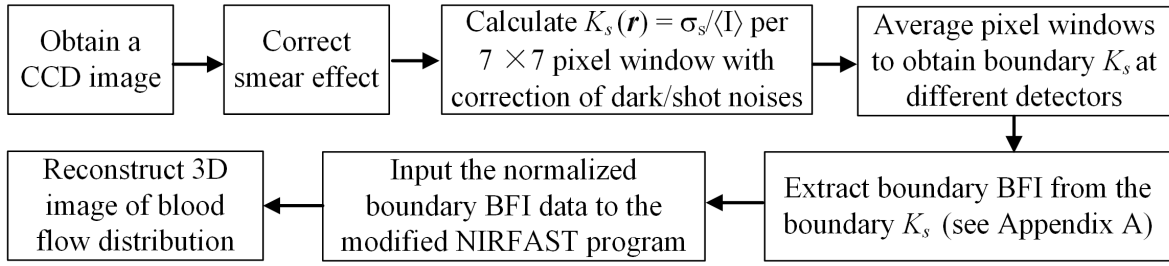
Fig. 2.   Flowchart of data processing sequence. The top left panel indicates the initial step of acquiring raw intensity images from the sample (e.g., phantom, tissue). The bottom left panel indicates the final resulting reconstructed image (3D tomographic flow distribution).
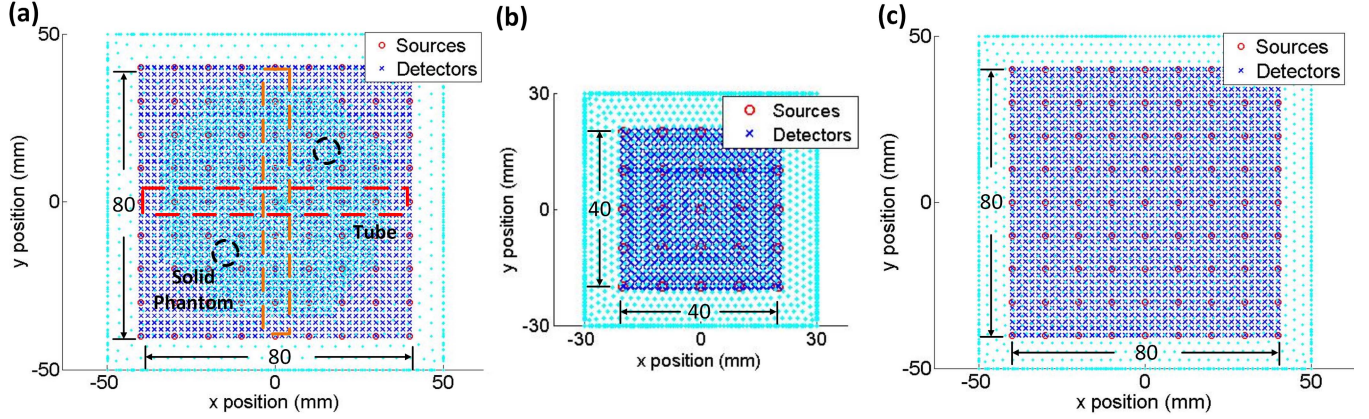

Fig. 3.   Source and detector configurations used by nc_scDCT for 3D flow imaging. Sources (circles) and detectors (crosses) were evenly distributed within an ROI to acquire boundary data. (a) An ROI of 80×80 mm^2 for tissue-simulating phantoms with flow tube placed at X or Y direction or spherical solid phantom anomalies. (b) An ROI of 40×40 mm^2 for forearm boundary data collection. (c) An ROI of 80×80 mm^2 was selected to image the incision area of mastectomy skin flap.

field autocorrelation function $g_1(r, \tau)$ [13], [14]:

$$\left[K_s(r)^2\right] = \frac{2\beta}{T} \int_0^T \left(1 - \frac{\tau}{T}\right) g_1^2(r, \tau) \, d\tau \qquad (2)$$

where T is the EMCCD exposure time and τ is the correlation delay time. β relates detector and speckle size, which can be determined experimentally from the measured correlation function curve. For the semi-infinite geometry, we substitute the appropriate form of $g_1(r, \tau)$ into (2) to obtain a nonlinear relationship between $BFI(r)$ and speckle contrast $K_s(r)^*$, i.e., $K_s^2(r) = f\left(\alpha D_B, T, \mu_a, \mu_s', \lambda, \beta, k_0, r\right)$. All parameters were known in the sense of being measured or taken from literature except $BFI(r)$. $BFI(r)$ refers to the combined term $\alpha D_B(r)$, where α is a unitless ratio of dynamic scatterers to total scatterers and $D_B(r)$ (unit: cm^2/s) is an effective diffusion coefficient of the moving scatterers. In biological tissues, primary dynamic scatterers detected by NIR techniques are moving red blood cells in the microvasculature. The remaining parameters include the tissue optical properties (i.e., tissue absorption coefficient $\mu_a(r)$ and reduced scattering coefficient $\mu_s'(r)$), source laser wavelength λ, and wavenumber k_0. The difference between the measured and theoretical speckle contrasts can then be minimized with respect to $BFI(r)$.

The complete sequence of steps from pre-processing of a CCD intensity image to the 3D tomographic flow result is

shown in **Fig. 2**. A diffuse tomographic instrument typically illuminates tissue and measures the diffusive light leaving the tissue with multiple sources and detectors projected on the measured tissue boundary. Only one source position is active for any given frame. **Fig. 3** shows the configurations of sources and detectors used in nc_scDCT for different experiments. For each source, images are acquired by the EMCCD camera with an exposure time T of 5 ms and frame rate of 2 frames/s. Central positions of the point sources illuminated by the galvo mirror are determined by extracting pixels with regional maximum intensities on EMCCD images. Raw images are corrected for smear effects of EMCCD frame transfer [13], [21]. From the corrected images, the measured $K_s(r)$ are then calculated using (1) as modified for instrumentation noises (i.e., shot noise and dark noise) [16], [22]. Multiple detectors are defined in the selected ROI and each detector includes 3×3 pixel windows (each window contains 7×7 pixels with a pixel size of 8 μm) [13]. Measured $K_s(r)$ are calculated per pixel window and those corresponding to a particular detector are averaged. These detectors are next averaged along frames to improve signal-to-noise ratio.

Boundary $BFI(r)$ are extracted using the measured and theoretical* $K_s(r)$ by minimization procedure. The BFIs are normalized to those taken from a homogenous Intralipid phantom with known BFI and optical properties for instrument calibration. Finally, the normalized boundary data (i.e., $g_1(r, \tau)$ at a single delay time $\tau = 3.2 \times 10^{-6}$s) along

---

*See Supplementary Material – Appendix A

with other known parameters are inserted into the modified NIRFAST program as developed previously for expedient FEM-based scDCT tomographic reconstructions [9].

B. Phantom Experimental Design

The use of tissue-simulating phantoms with known properties is a commonly accepted strategy for optical instrument calibration and validation. A homogeneous liquid phantom was firstly measured with nc_scDCT for instrument calibration. A tank was filled with the liquid phantom that consisted of distilled water, India ink (Black India, MA) and Intralipid (Fresenius Kabi, Sweden) (**Fig. 1a**). Intralipid particles in the liquid phantom provide control of scattering (μ_s') and Brownian motion (particle flow) while India ink controls absorption (μ_a). Optical properties of the homogeneous phantom were set as $\mu_a = 0.05$ cm^{-1} and $\mu_s' = 8$ cm^{-1} to match realistic tissues [13].

Following the calibration, two heterogeneous phantoms with increased or decreased flow contrast anomalies were used to validate the nc_scDCT system. In the first heterogeneous phantom [9], a transparent plastic cylindrical tube [dimension (mm): 6 (*Dia.*) $\times$ 80 (*L*)] with a very thin wall (< 0.5 mm) was placed at $\sim$5 mm (tube center to the ROI surface) into the background liquid phantom (**Fig. 1a**) along the X and Y directions respectively (**Fig. 3a**) to create high flow contrasts against the background. The tube was mostly filled with small pieces of solid phantom to randomize pumped particle motions as Brownian motion. The solid phantoms inside the tube were comprised of titanium dioxide, silicon and carbon black and had the same optical properties as the background liquid phantom (i.e., $\mu_a = 0.05$ cm^{-1} and $\mu_s' = 8$ cm^{-1}). A peristaltic pump (HV-77201-60, Cole Parmer, IL) connected in series with a hydraulic capacitor that damped fluid pulsations was employed to create step increases in steady flow from 0 to 20 ml/min at 5 ml/min increments within the tube placed along the X direction (**Fig. 3a**). For simplicity, only 20 ml/min pump speed was applied to the tube placed along the Y direction. Several soft rubber tubes (HV-06508-15, Cole-Parmer, IL) were used to connect the pump and plastic cylindrical tube and hold the cylindrical tube in the position. This liquid-liquid heterogeneous phantom enables easy updating of tissue properties in both the background and the anomaly.

In the second heterogeneous phantom [13], two sphere-shaped solid phantoms ($\mu_a = 0.05$ cm^{-1}, $\mu_s' = 8$ cm^{-1}, flow $= 0$) with a diameter of $\sim$7 mm were placed at $\sim$5 mm (sphere center to the ROI surface) into the background liquid phantom at the locations of X-Y planes (15, 15 mm) and (-15, -15 mm) respectively to create low flow contrasts against the background liquid phantom (**Fig. 3a**). A thin iron wire penetrating through the centers of the two sphere-shaped solid phantoms was used to hold the two anomalies in position.

For image reconstruction, an 80 $\times$ 80 mm^2 ROI on the focal plane was selected to cover the anomalies with high or low flow contrast (**Fig. 3a**). The galvo mirror delivered 830 nm light to 9 $\times$ 9 source locations inside the ROI with a total sampling time of $\sim$150 seconds. At each source location and

each pump speed, 4 frames of EMCCD images were taken and averaged. We defined 41 $\times$ 41 detectors evenly distributed in the ROI for image reconstruction. Image reconstructions were processed in a 100 $\times$ 100 $\times$ 30 mm^3 slab mesh centered at (0, 0, 15 mm) with 4 mm distance nodes and refined 1.3 mm distance nodes in the center to improve detection resolution ($\sim$60K nodes in total).

C. In Vivo Imaging of Forearm Blood Flow Distribution

We next tested this nc_scDCT instrument for continuous imaging of blood flow changes in a healthy human forearm [23] during a 4-minute arterial cuff occlusion protocol, approved by the University of Kentucky Institutional Review Board (IRB). An arterial cuff-occlusion with a pressure of 230 mmHg was applied for 4 minutes on the subject's upper arm to induce blood flow changes in the forearm (**Fig. 1b**). We adjusted the zoom lens of the EMCCD camera to image a ROI of 40 $\times$ 40 mm^2 on the subject's forearm (**Fig. 3b**). Then, 5 $\times$ 5 sources and 21 $\times$ 21 detectors were evenly distributed in the ROI for data collection with a total sampling time of $\sim$30 seconds. Image reconstruction was processed in a 60 $\times$ 60 $\times$ 30 mm^3 FEM slab mesh centered at (0, 0, 15 mm) with 2 mm distance nodes ($\sim$20K nodes in total).

D. Intraoperative Imaging of Mastectomy Skin Flap

We finally explored intraoperative imaging of a mastectomy skin flap using the nc_scDCT system. IRB approval for this prospective case study was obtained from the University of Kentucky. A female subject undergoing mastectomy through a skin sparing incision and immediate implant based breast reconstruction was studied. Intraoperative image was performed immediately after the mastectomy while the skin was closed temporarily using staples for the purpose of intraoperative measurement (**Fig. 1c**).

An 80 $\times$ 80 mm^2 ROI on the focal plane was selected to image the incision area (**Fig. 3c**). Then, 9 $\times$ 9 sources and 41 $\times$ 41 detectors were evenly distributed in the ROI for data collection with a total sampling time of $\sim$80 seconds. Two frames were collected and averaged for each source position. Image reconstruction was processed in a 100 $\times$ 100 $\times$ 30 mm^3 slab mesh centered at (0, 0, 15 mm) with 3 mm distance nodes ($\sim$16.5K nodes in total).

III. RESULTS

A. Phantom Validation

The phantom measurement protocol consisted of speckle contrast recovery over the liquid surface in a sequential manner for each of the 81 sources. For each source, 4 frames were acquired with an exposure time (T) of 5 ms and frame rate of 2 frames/s. The 41 $\times$ 41 detectors were defined resulting in S-D separations ranging from 0 to 113 mm (**Fig. 3a**). The homogeneous liquid phantom with a constant αD_B was measured first to evaluate and calibrate the nc_scDCT instrument. The boundary flow distributions over S-D links were recovered to determine the valid S-D separations for image
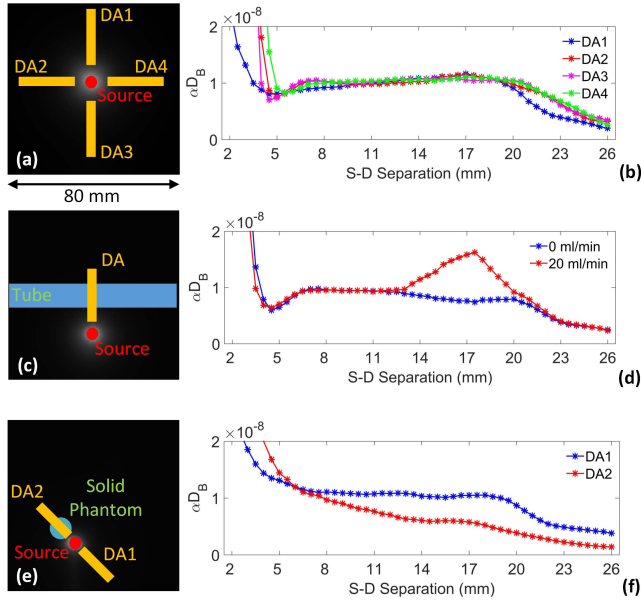
Fig. 4. Boundary flow index (αD_B) distributions over a selected single source and linear detector arrays (DAs). Each DA consisted of 49 detectors with an interval distance of 0.5 mm (2 to 26 mm). (a and b) In the homogeneous liquid phantom the boundary flow indices from 7 to 19 mm were fairly stable. (c and d) With tube placement, the higher flow inside the tube (20 ml/min) against background resulted in greater values in αD_B as detected at separations of 7 to 19 mm. (e and f) With spherical solid phantom placement, the zero flow in the solid resulted in lower values in αD_B as detected at separations of 7 to 19 mm.

reconstruction. For example, **Fig. 4b** illustrates boundary flow distributions with a selected source at the center of the homogeneous phantom and 4 detector arrays (DAs) across the central source (**Fig. 4a**). Each DA consisted of 49 detectors with an interval distance of 0.5 mm, resulting in multiple S-D separations ranging from 2 to 26 mm. Flow indices over the S-D separations from 7 to 19 mm were fairly stable (**Fig. 4b**); the means $\pm$ standard deviations of αD_B for DA1 to DA4 were $(1.04 \pm 0.09) \times 10^{-8}$, $(1.05 \pm 0.07) \times 10^{-8}$, (1.04 ± 0.04) $\times 10^{-8}$, and $(1.05 \pm 0.06) \times 10^{-8}$ cm^2/s, respectively. Similar results were also observed from other S-D links with the same range of S-D separations at different locations (data are not shown).

Fig. 4d shows boundary flow distributions with S-D links across the tube anomaly in the heterogeneous liquid-liquid phantom at the pumping speeds of 0 and 20 ml/min, respectively (**Fig. 4c**). Apparently, the higher flow inside tube (20 ml/min) against outside background resulted in greater values in αD_B, detected by corresponding effective S-D links. Similarly, **Fig. 4f** shows boundary flow distributions with S-D links outside (DA1) and across (DA2) the solid anomaly in the heterogeneous phantom, respectively (**Fig. 4e**). The zero flow in the solid sphere phantom resulted in lower values in αD_B, detected by corresponding effective S-D links. Based on these phantom testing results, we selected effective S-D links with the S-D separations ranging from 7 to 19 mm for image reconstructions in both phantom tests and later *in vivo* studies. Since the penetration depth of diffusive light is approximately one-half of the S-D separation
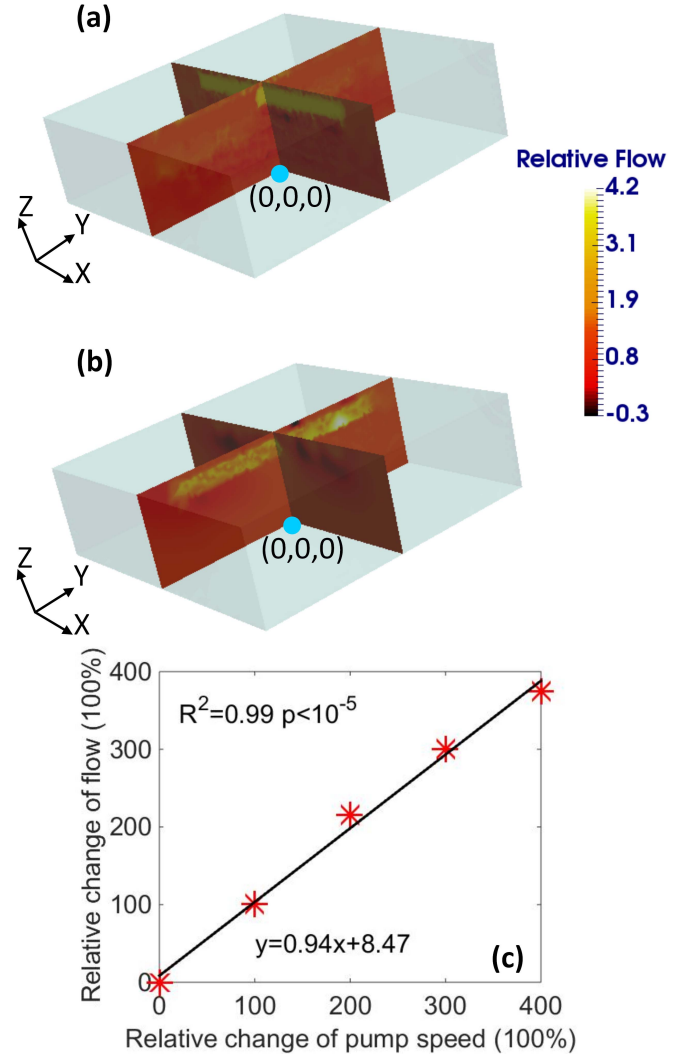

Fig. 5. The reconstructed 3D tube flow contrast images overlaid on the 2D cross-section views of X (a) and Y (b) directions respectively at a pump speed of 20 ml/min. The tube-shaped anomalies placed in different orientations were clearly recovered. (c) The reconstructed percentage flow changes accurately captured the relative flow changes in the pump-connected tube placed along X direction.

[24], [25], the nc_scDCT system can probe deep tissues up to ~10 mm.

Fig. 5a and **Fig. 5b** show the reconstructed 3D tube flow contrast images overlaid on the 2D cross-section views of X and Y directions respectively at a pump speed of 20 ml/min. Images are displayed with the open source visualization software of ParaView (Kitware, NY). Reconstructed flow heterogeneities were segmented by a half-maximum threshold [13] and the tube-shaped anomalies were clearly recognizable after image reconstruction. For percentage flow change comparison, the reconstructed anomaly flow changes were normalized to the averaged step difference of αD_B. The relationship between pumped flow (unit: ml/min) and particle motion (αD_B unit: cm^2/s) is complicated, but was confirmed linear [9]. As such, the pump speed changes were also normalized to the step difference (i.e., 5 ml/min). The reconstructed percentage flow changes accurately captured the relative flow changes in the
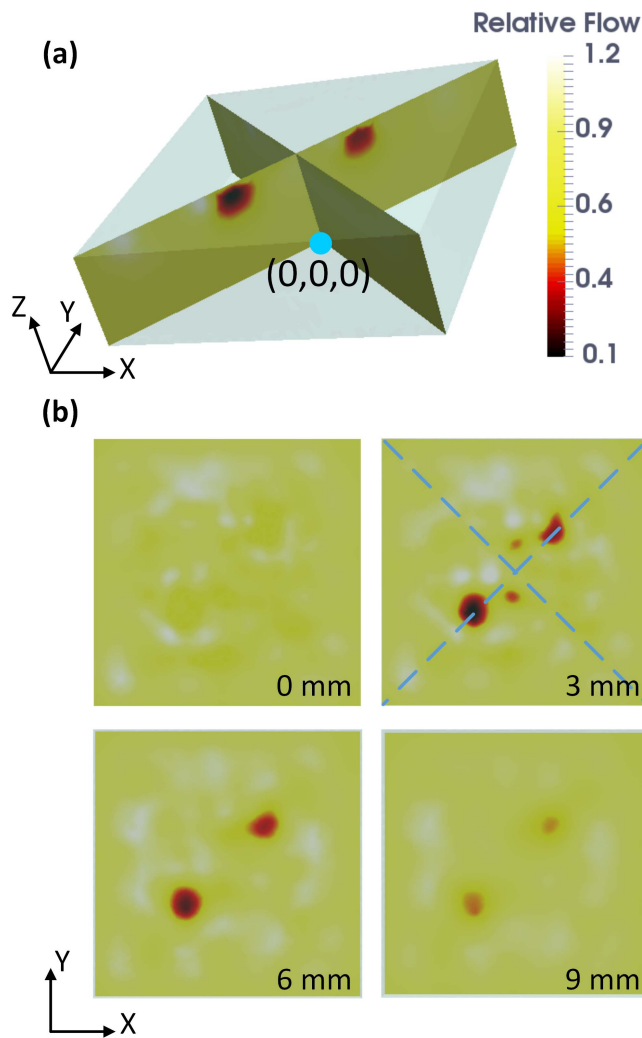
Fig. 6. (a) The reconstructed 3D flow contrast image of the two anomalies in the heterogeneous solid-liquid phantom overlaid on the 2D cross-section views. (b) The 2D cross-section views of X-Y plane at the depths of 0, 3, 6 and 9 mm below the phantom surface. The dashed lines shown in the upper-right subpanel of (b) illustrate the directions of 2D cross-section views shown in (a). The reconstructed heterogeneity locations and diameters agreed with those of solid sphere-shape phantoms inside the background liquid phantom.
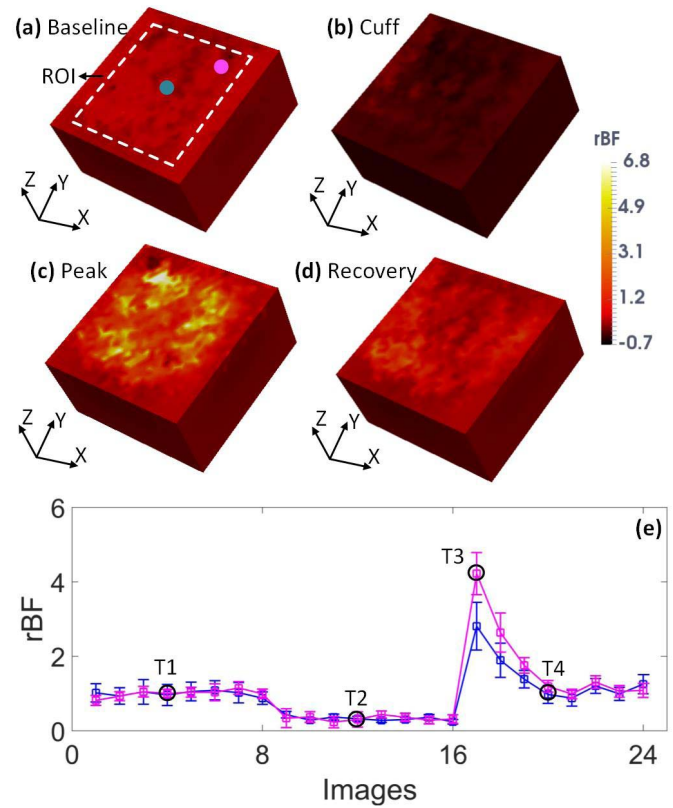

Fig. 7. The reconstructed 3D forearm blood flow images at the periods of baseline (a), cuff occlusion (b), reactive hyperemic peak flow (c), and recovery (d), respectively. (e) Blood flow changes relative to their baselines (i.e., rBF) over the period of occlusion protocol inside the selected two small tissue volumes of ~5 mm^3. Error bars represent the standard deviations of rBF values inside the small tissue volume. T1 to T4 represent the four time points corresponding to the images taken in (a) to (d). Although large spatial heterogeneity existed, rBF trends and variations throughout the occlusion protocol agree with physiological responses.

tube placed along X direction (linear regression: y = 0.94 × ± 8.47, R^2 = 0.99, and p < 10^{-5}, **Fig. 5c**). Notice again that only a constant pump speed of 20 ml/min was applied to the tube placed along the Y direction for simplicity.

Fig. 6a illustrates the reconstructed 3D flow contrast image of the two anomalies in the heterogeneous solid-liquid phantom overlaid on the 2D cross-section views. **Fig. 6b** shows the 2D cross-section views of X-Y plane at the depths of 0, 3, 6 and 9 mm below the phantom surface, respectively. Reconstructed flow heterogeneities were segmented by a half-maximum threshold resulting in averaged flow contrasts in the two anomalies of 0.32 and 0.25 (relative to a background flow value of ~1.00), which are comparable to our previous results found by similar solid-liquid phantoms [9], [13]. The reconstructed locations of the two anomalies centered at (14.2, 15.4, 24.5 mm) and (-14.4, -15.3, 25.8 mm), which were close to the actual

centers (15.0, 15.0, 25.0 mm) and (-15.0, -15.0, 25.0 mm), respectively. The reconstructed heterogeneity diameters were 8.6 and 7.1 mm respectively, which agreed fairly with the diameter of the solid sphere-shape phantoms (~7 mm).

B. Forearm Blood Flow Variation During Arterial Occlusion

Fig. 7 displays the reconstructed 3D forearm blood flow images at the periods of baseline (**Fig. 7a**), cuff occlusion (**Fig. 7b**), reactive hyperemic peak flow (**Fig. 7c**), and recovery (**Fig. 7d**). **Fig. 7e** shows time-course blood flow changes relative to their baselines (i.e., rBF) inside the selected two small tissue volumes of ~5 mm^3 centered at (0, 0, 25 mm) and (16, 16, 25 mm), respectively. The spatial averaged rBF values inside the two small tissue volumes at the four measurement time points (T1 to T4) as shown in **Figs. 7a-7d** were (96.1 ± 28.2% and 99.9 ± 11.6%), (32.3 ± 6.5% and 30.4 ± 20.5%), (280.8 ± 63.9% and 422.0 ± 56.6%), and (97.3 ± 23.8% and 119.2 ± 15.7%), respectively. Apparently, large spatial heterogeneity existed in rBF responses to the arterial occlusion. However, rBF trends and variations throughout the occlusion protocol agreed well
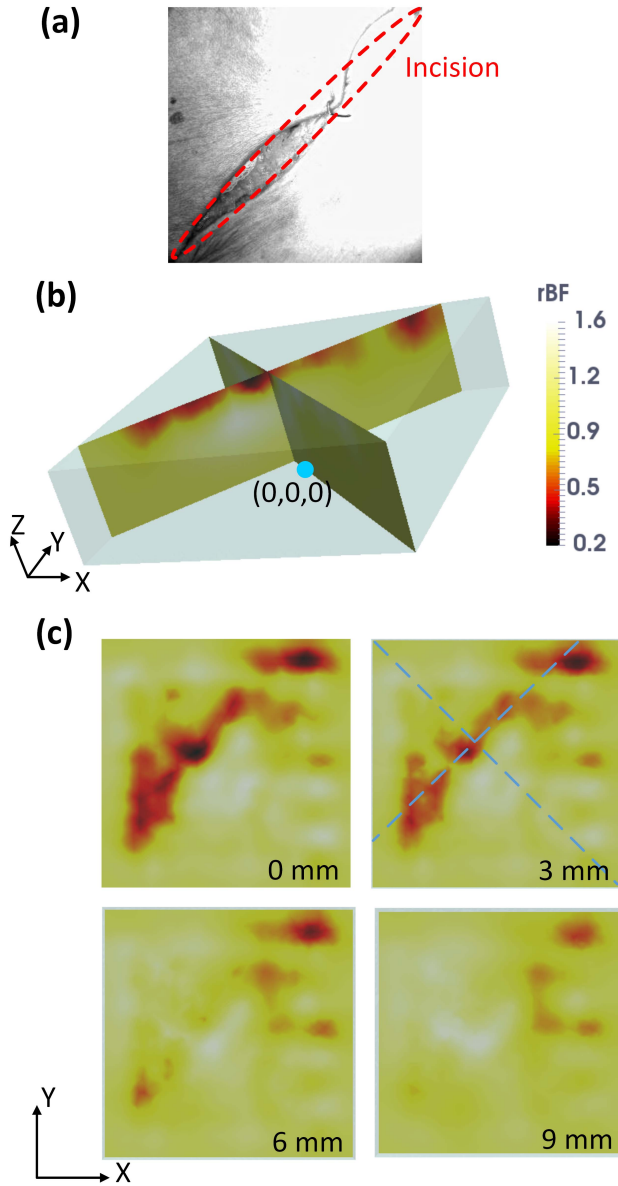
Fig. 8.   Intraoperative imaging of a mastectomy skin flap. (a) A photograph of a mastectomy skin flap taken by the EMCCD camera. (b) The reconstructed 3D blood flow contrast image overlaid on the 2D cross-section views of the mastectomy skin flap. (c) The 2D cross-section views of X-Y plane at the depths of 0, 3, 6 and 9 mm below the mastectomy skin flap surface. The dashed lines shown in the upper-right subpanel of (c) illustrate the directions of 2D cross-section views shown in (b). The ischemic areas with lower rBF values were observed around the incision margin of the mastectomy skin flap.

with our previous results [7], [23]. These results demonstrate the feasibility of nc_scDCT for 3D *in vivo* imaging of blood flow distributions in deep tissue volumes.

C. Blood Flow Distribution in Mastectomy Skin Flap

Fig. 8b illustrates the reconstructed 3D blood flow contrast image overlaid on the 2D cross-section views of a mastectomy skin flap. **Fig. 8c** shows the 2D cross-section views of X-Y plane at the depths of 0, 3, 6 and 9 mm below the mastectomy skin flap surface, respectively. Large spatial

heterogeneity in rBF existed and ischemic areas with lower rBF values were observed around the incision margin of the mastectomy skin flap (**Fig. 8a**).

IV. DISCUSSION AND CONCLUSIONS

We have developed a novel fully noncontact CCD-based nc_scDCT system (**Fig.1** and **Fig. 3**) that can probe deep tissue (~10 mm depth) 3D flow distributions in the reflectance configuration with an adjustable ROI, rapid and robust data acquisition potential, and flexible S-D arrangements. This design leverages advancements made previously from our scDCT prototype implementation [13]. The benefits of reflectance-based operation are retained and common among both systems: scDCT and nc_scDCT. These benefits include promoting high translatability between small animal and large human subjects and increasing the applicability to large subjects where transmission is not feasible. The FEM-based image reconstruction method is also a common feature which works with simple geometry as well as for tissues with complex surface geometries if a 3D surface outline can be acquired and incorporated, as were presented in our previous works [10], [19].

The nc_scDCT system achieves several unique features over its predecessors. The innovation exclusive to nc_scDCT is bringing the incipient reflectance diffuse speckle contrast-based technique to a fully noncontact scheme by means of modifying the laser source to tissue transport mechanism. The removal of contact source fibers by means of a directable galvo mirror beam eliminates the complications encountered due to undesirable contact interactions between the hardware components and tissue such as compression and potential infection. The resulting system has a lower cost than contact based alternatives due to avoidance of optical fibers and reduces the overall number of components. The galvo mirror removes the static source constraint of the prototypical scDCT instrument. The available data density rises significantly as a result and source positions are now possible within the FOV. The future sequencing of the galvo mirror with the scDCT optical switch could provide further expansion such as into single instrument multimodal optical measurements.

The highly sensitive, multitudinous pixel grid detection element greatly increases the available detectors and allows for rapid data acquisition (< 1s per frame). In concert with the speckle contrast flow technique the situation of numerous individual, slow sampling and expensive avalanche photodiodes connected to optical fibers can be avoided. Additionally, the motion artifacts and lengthy scan time (~25 min) from mechanical scanning with our previous fully noncontact DCT (ncDCT) instrument based on APD detection are mitigated with the new diffuse speckle contrast flow measurement and CCD setup.

The major innovations nc_scDCT provides over its progenitors become apparent when considering the inherited scDCT capabilities and newly integrated features collectively. The first unique capability is the adaptable arrangement and density of S-D pairs due to the CCD detection and galvo mirror source guidance. The source locations were strictly outside

the FOV in the scDCT design. This limited possible S-D patterns and inhibited adequate sampling from the center of the FOV. In the current study we intersperse the sources (e.g., 9×9 or 5×5 as tested) within the detector field (e.g., 41×41 or 21×21 as tested) in a grid to sample equally among the expected heterogeneous and homogeneous contrast areas. However, the system exhibits the potential for more complex S-D arrangements based on future application. The boost in source/detector quantity and the S-D configurations now supplies, typically, from hundreds to tens of thousands of pairs. Comparatively, the cost and physical limitations of employing many optical fibers and/or APD's do not scale well for robust and dense S-D potential. The second unique nc_scDCT capability is the flexible ROI which works in conjunction with the aforementioned benefits to enable scalability between applications. Coupling the S-D options with the zoom lens provides for tailoring the system parameters to maximize operation under small and large ROI's (within the context of diffuse optics; on the order of cm) with varying application-specific constraints (e.g., 80×80 mm^2 or 40×40 mm^2 ROI's as tested). These enhancements combine to produce a fast, continuous, portable, noncontact, noninvasive, high sampling density instrument and is an important step towards the *in vivo*/clinical application, especially intraoperative cases where prompt collection is required for the noncontact measurement of vulnerable tissues. Additionally, the system lends itself to immediate extension to hybrid instruments combining related optical techniques including planar and diffuse fluorescence measurement, LSCI of superficial blood flow, and diffuse optical spectroscopy and tomography (DOS/DOT) for chromophore concentrations.

We have calibrated and validated the nc_scDCT system using tissue phantoms with two types of heterogeneities (high and low flow contrasts respective to the background flow) and a change in orientation. Results indicate the sufficiency of our identification of an adequate S-D range and response to heterogeneity presence (**Fig. 4**), and that both cases of flow contrast were successfully reconstructed and heterogeneity characterized (**Fig. 5** and **Fig. 6**). The recovered relative flow contrast change in the inserted cylindrical tube was highly correlated to the pump speed change ($R^2 = 0.99$, and $p < 10^{-5}$) demonstrating that we accurately captured the relative flow changes in the tube (**Fig. 5**). After changing the orientation of the tube we found that the system was also able to detect and show such modification. The recovered relative flow contrast of the solid phantoms were 0.25 and 0.32 to the background (~ 1.00) (**Fig. 6**), which are comparable to our previous results found by similar phantoms [9], [13]. Their localization matched our expectations with regard to their arrangement in the liquid phantom background, depth (2% and 3.2% errors), and diameter (1.4% and 23% errors).

With the phantom tests supporting device functionality we then tested it for *in vivo* images, especially that of intraoperative imaging which requires the advantages of a fast, portable, and high resolution system. Results from *in vivo* imaging indicate the capability of nc_scDCT to monitor deep tissue blood flow distributions of both temporal (forearm) and spatial (forearm, mastectomy skin flap) variations including

clinical utilization. The well-known hyperemic response after cuff occlusion was clearly visible at multiple locations in the forearm tissue (**Fig. 7**). Previous studies have used varied occlusion times ranging from 3 to 5 minutes to create significant hemodynamic variations in the occluded tissues [7], [17], [23]. A longer occlusion time results in more sampling data points (when using a fixed sampling rate) and stronger reactive hyperemia after the release of occlusion, which can be more easily detected by our imaging system. Additionally, the tissue collectively trended to a low flow state and high flow state in response to the cuff status. The apparent random spatial variation in response is expected due to regional hemodynamic response differences in the individual subject. A more accurate picture of this result may be accomplished by monitoring additional subjects of both a healthy and diseased nature.

The application to mastectomy skin flap was the most notable achievement. We found an obvious blood flow decrease at the edge of the mastectomy skin flap in the same orientation and shape as the perceptible site in the plain image (**Fig. 8**). This information could, after further studies in a large patient population, optimize the surgical procedure for the patient, e.g., providing intraoperative guidance of compromised tissue removal to prevent flap necrosis. We emphasize here that the sensitivity of NIR diffuse optical technologies is primarily of large/deep volumes of tissue rather than individual vessels. The spatial resolution can typically be considered $\sim 20\%$ of the light penetration depth [26] which is approximately one half of the S-D distance [27]. Correspondingly, our nc_scDCT system with a maximal S-D distance of ~ 20 mm should have a spatial resolution of ~ 1 mm on the tissue surface and of ~ 2 mm at the depth of ~ 10 mm. Future studies will comprehensively characterize the performance of the nc_scDCT system including the spatial resolution using tissue phantoms with anomalies at different depths and with different sizes (see a similar analysis for our ncDCT [19]).

We note a few limitations in respect to the current system and study. The effective range appeared to be limited to between 7 mm to 19 mm which may be due to several reasons. First, optical diffraction causes a relatively large source spot size that affects the speckle contrast within short S-D distances (e.g., < 7 mm). Second, the sensor quantum efficiency is not high in NIR range ($< 40\%$ in our EMCCD camera for 830 nm), resulting in relatively low signal/noise ratio at large S-D distances (e.g., > 19 mm). We have successfully reproduced the experimental heterogeneities despite these limitations by combining numerous S-D pairs and determining an accurate dynamic range. The possibility of extending the dynamic range will be part of our future work to improve the system. Although the data collection by the nc_scDCT is fast (~ 1 minutes), the current imaging reconstruction technique is itself a slow process inhibiting the real time usage of the results. These stem in part from the process of acquiring the boundary surface geometry information and the processing requirements for solving the inverse problem for image reconstruction. These limitations may be mitigated to some extent with the PhotoMetrix technique [28] for rapid geometry measurement and modified fast algorithms (<7 minutes for

our mesh node number) for real time analysis [29]. The data collection time was restricted to 2 frames/s in this study to stabilize the signal collected. Removal of this constraint can be accomplished with further investigation using high quality cameras.

In conclusion, the nc_scDCT system is an advanced technology for noninvasive, fast, cost-effective, portable 3D blood flow imaging. The noncontact reflectance configuration with a flexible ROI was shown adaptable to multiple different applications as exemplified by our imaging in phantoms, forearm, and reconstructive flap. The imaging capability was validated by heterogeneous tissue-like phantoms with flow contrasts both greater and lesser than background flow. The clinical viability of the system was also proven as evidenced by forearm cuff-occlusion and intraoperative mastectomy outcomes. This study demonstrates a solid step towards blood flow imaging of large and deep tissue volumes in clinical settings (e.g., intraoperative monitoring of breast reconstruction after mastectomy and diagnosis of ulcerous/wound/burn tissues).

ACKNOWLEDGMENT

REFERENCES

[1] D. A. Boas and A. K. Dunn, "Laser speckle contrast imaging in biomedical optics," *J. Biomed. Opt.*, vol. 15, p. 011109, Jan./Feb. 2010.

[2] A. F. Fercher and J. D. Briers, "Flow visualization by means of single-exposure speckle photography," *Opt. Commun.*, vol. 37, no. 5, pp. 326–330, 1981.

[3] D. A. Boas and A. G. Yodh, "Spatially varying dynamical properties of turbid media probed with diffusing temporal light correlation," *J. Opt. Soc. Amer. A, Opt. Image Sci., Opt. Image Sci.*, vol. 14, pp. 192–215, Jan. 1997.

[4] D. A. Boas, L. E. Campbell, and A. G. Yodh, "Scattering and imaging with diffusing temporal field correlations," *Phys. Rev. Lett.*, vol. 75, pp. 1855–1858, Aug. 1995.

[5] C. Zhou, G. Yu, D. Furuya, J. H. Greenberg, A. G. Yodh, and T. Durduran, "Diffuse optical correlation tomography of cerebral blood flow during cortical spreading depression in rat brain," *Opt. Exp.*, vol. 14, pp. 1125–1144, Feb. 2006.

[6] A. Yodh and B. Chance, "Spectroscopy and imaging with diffusing light," *Phys. Today*, vol. 48, pp. 34–40, Mar. 1995.

[7] Y. Shang, Y. Zhao, R. Cheng, L. Dong, D. Irwin, and G. Yu, "Portable optical tissue flow oximeter based on diffuse correlation spectroscopy," *Opt. Lett.*, vol. 34, pp. 3556–3558, Nov. 2009.

[8] C. Huang *et al.*, "Noncontact diffuse optical assessment of blood flow changes in head and neck free tissue transfer flaps," *J. Biomed. Opt.*, vol. 20, p. 075008, 2015.

[9] Y. Lin, C. Huang, D. Irwin, L. He, Y. Shang, and G. Yu, "Three-dimensional flow contrast imaging of deep tissue using noncontact diffuse correlation tomography," *Appl. Phys. Lett.*, vol. 104, p. 121103, Mar. 2014.

[10] C. Huang, Y. Lin, L. He, D. Irwin, M. M. Szabunio, and G. Yu, "Alignment of sources and detectors on breast surface for noncontact diffuse correlation tomography of breast tumors," *Appl. Opt.*, vol. 54, pp. 8808–8816, Oct. 2015.

[11] H. Cheng, Q. Luo, S. Zeng, S. Chen, J. Cen, and H. Gong, "Modified laser speckle imaging method with improved spatial resolution," *J. Biomed. Opt.*, vol. 8, pp. 559–564, Jul. 2003.

[12] S. Yuan, A. Devor, D. A. Boas, and A. K. Dunn, "Determination of optimal exposure time for imaging of blood flow changes with laser speckle contrast imaging," *Appl. Opt.*, vol. 44, pp. 1823–1830, Apr. 2005.

[13] C. Huang *et al.*, "Speckle contrast diffuse correlation tomography of complex turbid medium flow," *Med. Phys.*, vol. 42, no. 7, pp. 4000–4006, 2015.

[14] R. Bi, J. Dong, and K. Lee, "Deep tissue flowmetry based on diffuse speckle contrast analysis," *Opt. Lett.*, vol. 38, pp. 1401–1403, May 2013.

[15] H. M. Varma, C. P. Valdes, A. K. Kristoffersen, J. P. Culver, and T. Durduran, "Speckle contrast optical tomography: A new method for deep tissue three-dimensional tomography of blood flow," *Biomed. Opt. Exp.*, vol. 5, pp. 1275–1289, Apr. 2014.

[16] C. P. Valdes, H. M. Varma, A. K. Kristoffersen, T. Dragojevic, J. P. Culver, and T. Durduran, "Speckle contrast optical spectroscopy, a non-invasive, diffuse optical method for measuring microvascular blood flow in tissue," *Biomed. Opt. Exp.*, vol. 5, pp. 2769–2784, Aug. 2014.

[17] M. Seong *et al.*, "Simultaneous blood flow and blood oxygenation measurements using a combination of diffuse speckle contrast analysis and near-infrared spectroscopy," *J. Biomed. Opt.*, vol. 21, p. 27001, Feb. 2016.

[18] C. Huang *et al.*, "Low-cost compact diffuse speckle contrast flowmeter using small laser diode and bare charge-coupled-device," *J. Biomed. Opt.*, vol. 21, no. 8, p. 080501, 2016.

[19] L. He, Y. Lin, C. Huang, D. Irwin, M. M. Szabunio, and G. Yu, "Noncontact diffuse correlation tomography of human breast tumor," *J. Biomed. Opt.*, vol. 20, no. 8, p. 086003, 2015.

[20] D. D. Duncan, S. J. Kirkpatrick, and R. K. K. Wang, "Statistics of local speckle contrast," *J. Opt. Soc. Amer. A, Opt. Image Sci.*, vol. 25, pp. 9–15, Jan. 2008.

[21] W. Ruyten, "Smear correction for frame transfer charge-coupled-device cameras," *Opt. Lett.*, vol. 24, pp. 878–880, Jul. 1999.

[22] S. Yuan, "Sensitivity, noise and quantitative model of laser speckle contrast," Ph.D. dissertation, Dept. Biomed. Eng, Tufts Univ., Medford, MA, USA, 2008.

[23] Y. Lin, L. He, Y. Shang, and G. Yu, "Noncontact diffuse correlation spectroscopy for noninvasive deep tissue blood flow measurement," *J. Biomed. Opt.*, vol. 17, p. 010502, Jan. 2012.

[24] S. Fantini, M. A. Franceschini, and E. Gratton, "Semi-infinite-geometry boundary-problem for light migration in highly scattering media—A frequency-domain study in the diffusion-approximation," *J. Opt. Soc. Amer. B, Opt. Phys.*, vol. 11, pp. 2128–2138, Oct. 1994.

[25] D. Irwin *et al.*, "Influences of tissue absorption and scattering on diffuse correlation spectroscopy blood flow measurements," *Biomed. Opt. Exp.*, vol. 2, pp. 1969–1985, Jul. 2011.

[26] L. V. Wang, H. I. Wu, and W. Wang, *Biomedical Optics: Principles and Imaging*. Hoboken, NJ, USA: Wiley, 2007.

[27] G. Yu, T. Durduran, C. Zhou, R. Cheng, and A. Yodh, "Near-infrared diffuse correlation spectroscopy (DCS) for assessment of tissue blood flow," in *Handbook of Biomedical Optics*, D. Boas, C. Pitris, and N. Ramanujam, Eds. New York, NY, USA: Taylor & Francis, 2011, pp. 195–216.

[28] Y. Zhang, G. M. Gibson, R. Hay, R. W. Bowman, M. J. Padgett, and M. P. Edgar, "A fast 3D reconstruction system with a low-cost camera accessory," *Sci. Rep.*, vol. 5, 2015, Art. no. 10909.

[29] X. Wu, A. T. Eggebrecht, S. L. Ferradal, J. P. Culver, and H. Dehghani, "Fast and efficient image reconstruction for high density diffuse optical imaging of the human brain," *Biomed. Opt. Exp.*, vol. 6, pp. 4567–4584, Nov. 2015.